Hindawi Publishing Corporation
International Journal of Rotating Machinery
Volume 2016, Article ID 3458750, 12 pages
http://dx.doi.org/10.1155/2016/3458750

Research Article

Flettner Rotor Concept for Marine Applications: A Systematic Study

A. De Marco, S. Mancini, C. Pensa, G. Calise, and F. De Luca

Department of Industrial Engineering, University of Naples Federico II, Via Claudio 21, 80125 Naples, Italy

Correspondence should be addressed to S. Mancini; simone.mancini@unina.it

Received 19 January 2016; Revised 31 May 2016; Accepted 15 June 2016

Academic Editor: Ryoichi Samuel Amano

The concept of Flettner rotor, a rotating cylinder immersed in a fluid current, with a top-mounted disk, has been analyzed by means of unsteady Reynolds averaged Navier-Stokes simulations, with the aim of creating a suitable tool for the preliminary design of the Flettner rotor as a ship's auxiliary propulsion system. The simulation has been executed to evaluate the performance sensitivity of the Flettner rotor with respect to systematic variations of several parameters, that is, the spin ratio, the rotor aspect ratio, the effect of the end plates, and their dimensions. The Flettner rotor device has been characterized in terms of lift and drag coefficients, and these data were compared with experimental trends available in literature. A verification study has been conducted in order to evaluate the accuracy of the simulation results and the main sources of numerical uncertainty. All the simulation results were used to achieve a surrogate model of lift and drag coefficients. This model is an effective mathematical tool for the preliminary design of Flettner rotor. Finally, an example of assessment of the Flettner rotor performance as an auxiliary propulsion device on a real tanker ship is reported.

1. Introduction

In the era in which most of the world's attention is focused on improving energy savings, the use of spinning cylinders as an auxiliary naval propulsion system has become a reality. Flettner rotors are rotating cylinders that, when immersed in a fluid stream, are able to produce fluid dynamic lift using the Magnus effect. This idea is due to the German engineer Anton Flettner who studied in the 1920s the effectiveness of spinning cylinders as a ship's propulsion system. This kind of propulsion systems was enrolled for the first time in 1925-1926 on the Buckau ship, shown in Figure 1(a). This ship used two rotors to augment the propulsion power of its former conventional sailing rigs. However, further commercial development of the FRs did not take place before the twenty-first century. Nowadays, with increasing fuel prices and a general growing sensibility about green and environmental-protection policies, the FRs are being seriously reconsidered as viable green ship propulsion devices. In 2010, Enercon, a wind energy company, launched a Flettner-powered cargo ship named E-Ship 1, Figure 1(b). On E-Ship 1 the FRs are used to assist the diesel engine: as reported in the Enercon technical report [1], the owner declares that thanks to this device a 30% reduction of fuel consumption is achieved. E-Ship 1 is in current use and has been recounted to cover more than 17000 sea miles with no mention of particular problems about the FRs [1].

2. Literature Overview

The capability of infinite length rotating cylinders to produce aerodynamic forces was studied for the first time at the Langley NACA Laboratory by Reid [2]; he found that in particular conditions such simple devices are capable of developing very high values of the lift coefficient and of the aerodynamic efficiency (i.e., the lift-to-drag ratio). Thom [3] presented an experimental work on rotating cylinders, with emphasis on the effects of the Reynolds number (Re), surface conditions, aspect ratio, and end plates disks, describing the device in terms of lift, drag, and torque coefficients. Successively, Swanson [4] clarified the physics underpinning the FR, thus highlighting the nature of the circulation around the rotating cylinder. More recently, a comprehensive study

(a) (b)

Figure 1: Buckau, first Flettner's ship (a), and E-Ship 1 by Enercon wind company (b).

on the functioning of FR was conducted by Da-Qing et al. [5]. This work presents a numerical study of aerodynamic performance of Flettner rotors at a high Re ($1.6 \cdot 10^6$) in relation to the change of spin ratio (SR) and aspect ratio (AR). Special attention is paid to the formation of vortex structures and the relationship between wake instability and fluctuation of aerodynamic loads. This paper also reports statistical expressions correlating C_L and C_D with SR.

The aerodynamic coefficients of an FR depend on various parameters (geometrical and functional). In the following subsections the most important parameters are briefly summarized.

2.1. Spin Ratio. The amount of aerodynamic force generated by a rotating cylinder, that is, an FR, is mainly dependent on the SR (or velocity ratio, also named α), which accounts for the angular speed Ω, the FR diameter d, and the free stream velocity U, as shown in Figure 2. The flow phenomena around a 3D circular cylinder are rather complex and feature both tip vortices and an alternate vortex shedding between the rotor sides. Seifert [6] highlights that vortex shedding occurs for Re all the way up to at least $8.0 \cdot 10^6$ and that the extension of the vortices depends also on the Strouhal number (St). The St represents the degree of unsteadiness of the oscillating flow past the rotating cylinder. In Mittal and Kumar [7], a detailed analysis of St regimes for rotating cylinders is presented. Low Strouhal numbers ($St < 10^{-4}$) indicate long eddy formations; hence, the flow is considered quasi-steady. According to Badalamenti and Prince [8], the shedding phenomena are also influenced by SR: small spin ratios cause long eddy formations, while higher SRs cause considerably short eddies. Thus, the Kàrman vortex street is seen for $SR \leq 2$ when large eddies are formed and shed alternately on the two sides of the cylinder. Conversely, vortex formation and shedding can no longer be seen for $2.0 \leq SR < 3.0$, and for $3.0 \leq SR < 3.5$ quasi-steady-states are observable. At $SR = 3.5$ a second shedding mode is found.

Swanson [4] pointed out that lift and drag of a rotating cylinder at $SR < 1.0$ show a significant dependency on Re. The effects of Re are more evident on lift at $Re > 6{\times}10^4$, which is also confirmed by Gowree and Prince [9]. When $SR > 2.5$ and $Re > 4 \times 10^4$, drag and lift curves have a slightly growing trend for increasing Re.

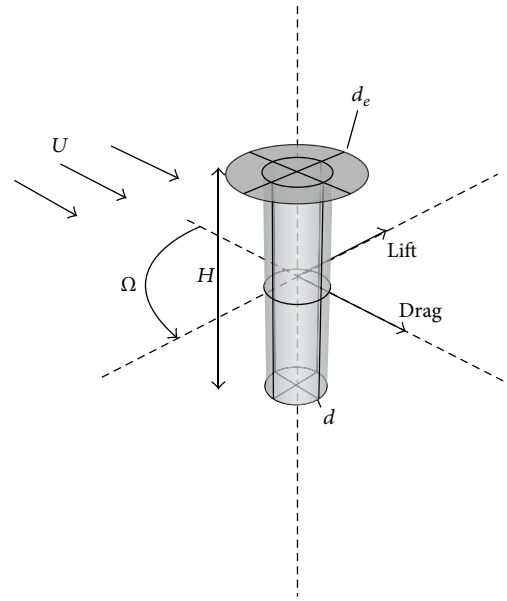

Figure 2: Sketch of the FR with end plate and main relevant parameters.

2.2. Aspect Ratio. The main shape factor of an FR is the aspect ratio AR, which significantly influences the FR effectiveness in producing aerodynamic forces. The AR of FR device, which is the ratio between height and diameter, modifies its aerodynamic efficiency, as for higher aspect ratios the FR device behaves much like a wing, with tip vortices that take part in the lift production. An important consideration is presented by Swanson [4], who observed that the smaller the aspect ratio the smaller the maximum lift obtained and the smaller the velocity ratio at which this maximum is reached. Swanson also demonstrated that, for very high aspect ratio, the lift can reach higher values than the maximum theoretical limit predicted by Prandtl's classical theory [10]. An extensive comparison of the main data available in the literature on FR

performances, both experimental and numerical ones, along with some considerations, can be found in De Marco et al. [11].

2.3. End Plate. The idea of applying an end plate on FR to optimize its aerodynamic efficiency was first suggested by Prandtl [10]. The presence of an end plate modifies the 3D flow phenomena at the tip of the FR, augmenting the "effective AR" of the rotor. Thom [3] investigated the effect of large end plates with a diameter ratio $d_e/d = 3.0$, where d_e is the diameter of the end plate disk (Figure 2).

The FR with end plate, also called Thom disk, is able to produce almost double the lift at high velocity ratios; for example, SR = 2.0. In Badalamenti and Prince [12] it is shown that for a cylinder with AR = 5.1 and diameter ratios ranging from 1.1 to 3.0, the effects of the increases d_e/d and AR are similar. Increasing the d_e/d value, a higher lift value is generated by the FR and such value occurs at higher SR as well (see Seifert [6]). Thouault et al. [13] presented a detailed analysis of the effects of end plate dimensions on the FR efficiency, based on experiments and numerical simulations.

A discussion of how the end plate size is related to SR in order to achieve optimal performances of the FR is presented by Seifert [6]. In his work Seifert observes that at low spin ratio (SR = 1.0) smaller plates generally give lightly smaller drag; for applications at moderate spin ratio ($1.0 < SR < 3.0$) larger plates are preferred, so as to delay the increase in induced drag, while, for high spin ratio applications ($SR > 3.0$), smaller plates are again more desirable.

2.4. Marine Application of FR. Concerning the use of FR for marine applications, not many research papers are available in the literature. An overview of the applications of the Magnus effect devices in the marine field is given in Morisseau [14]. The Magnus effect devices can be used as roll stabilizers, water propellers, and air generator, such as FR. Moreover this paper reports an interesting preliminary analysis of retrofitting of a single screw US Navy auxiliary ship with five FRs. More recently, in Pearson [15], a "first-stage" assessment is found in practical limitations as well as negative side effects of retrofitting Flettner rotors to a ship. All these considerations are collected in order to create a software model for a preliminary analysis of the viability of retrofitting FR to a defined ship, before any progression onto analyzing specific scenario benefits or other detailed investigations. A limit of this work is in the estimation of FR performances, which are evaluated only as a function of SR. The software presented assumes a universal FR geometry, with $d_e/d = 1.5$ and AR = 5 (based on Prandtl's study [10]) and evaluates C_L and C_D of this FR; then, the performances of FR are evaluated changing SR in the range 0.0~8.0.

Traut et al. [16] explore the potential for harnessing wind power for shipping applications. Numerical models of the two main wind power technologies, FR and towing kite, are linked with wind data along a set of five trade routes. The results of their analysis give an estimation of the average wind power contribution on a defined route. For a single FR, the delivered power is in a range between 193 and 373 kW and, for the towing kite, between 127 and 461 kW. The FR has a variability of the delivered power smaller than the towing kite, due to the different dependencies on wind speed and direction. The average power contribution coming from an FR is higher than that coming from the kite on some routes and lower on others. But an advantage of FR is that the contribution would be expected to increase almost linearly with the number of devices installed on the same ship (in this respect, a quantitative study of interference effects is lacking in the literature). For this reason, for instance, installing three FRs on a 5500 DWT (dead weight tonnage) general cargo carrier could provide, on average, more than half the power required by the main engine under typical slow steaming conditions.

Figure 3: Estraden ship: latest FR installation.

2.5. Aim of the Work. The present research extends previous investigations presented in De Marco et al. [17] and in De Marco et al. [11] in order to assess, in a systematic way, the effect of the FR key parameters, that is, the AR, SR, and the end plate diameter, on the device performance. Furthermore, the mutual interaction effects of these parameters on the aerodynamic forces generated by FR are investigated. The analyzed ranges of variation of the key parameters have been chosen considering technologically plausible marine applications of the FR concept.

3. Flettner Rotor Installations and Reference Data

To choose the ranges of the key parameters some constraints have been taken into account. For instance one has to consider the currently available technology as well as the practicality in marine applications. Another important factor is the vortex shedding risk (first and second mode) which depends on the mutual interaction between AR and SR. Consequently the limits of AR and SR have been identified by the analysis of some real FR installations on board.

The known installations of FR and their reference data are summarized in Table 1. The first two examples, Buckau and Barbara, are not in service, while the two ships, E-Ship-1 and Estraden (Figure 3), are currently operated by North European owners for commercial purposes. In all of these examples a Thom disk is used and the AR are in the range 5.5~7.0. This range is taken as a reference for the

Table 1: Geometric, performance, and structural related parameters collected from all-known rotor ships.

Ship (year)	Buckau (1924)	Barbara (1926)	E-Ship 1 (2010)	Estraden (2014)
Type	Retrofit	Newbuild	Newbuild	Retrofit
Height (m)	15.6	17.0	27.0	19.0
Diameter (m)	2.8	4.0	4.0	3.0
Aspect ratio	5.6	4.3	6.8	6.3
End plate	Yes	Yes	Yes	Yes
Material	Zinc coated steel	Aluminum	NA	Composite
Max rpm	135.0	150.0	NA	250.0

Table 2: Values of analyzed variables.

Variables	Values			
SR	1.0	1.5	2.0	3.0
AR	2.0	4.0	6.0	8.0
d_e/d	1.0	2.0	3.0	/

investigations presented here. It is observed that the angular rotor speeds have increased over the years, thus allowing higher SR. However the SR values of interest for marine application remain in the range 1.0 to 3.0. For example, SR = 2.5 is obtained for a typical relative wind velocity of 20 kn (10 m/s), a reasonable diameter of 3.0 m, and a rotation speed of 160 rpm.

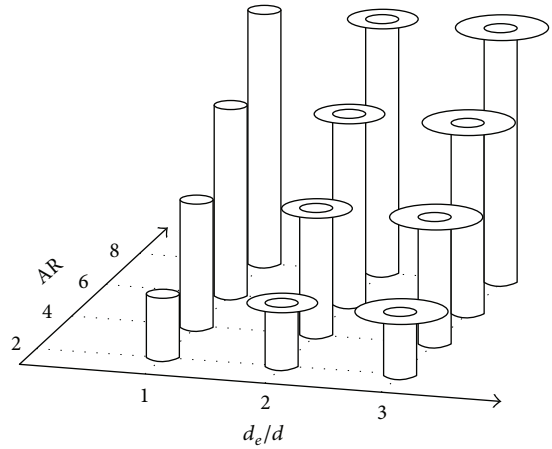

Figure 4: Sketch of all geometry of FRs tested.

4. Numerical Experiments

Systematic variations of FR configurations have been investigated by means of URANS simulations in incompressible flow. All the analyses have been performed using the commercially available computational fluid dynamics software CD adapco STAR-CCM+ v. 9.06. The simulations were conducted using the same approach, such as the overset/chimera grid technique, described in De Marco et al. [17] and in De Marco et al. [11]. Furthermore fairly wide ranges of the key parameters, that is, AR, SR, and d_e/d, have been examined, as detailed in the Table 2 and displayed in Figure 4. The characteristics of FRs were evaluated in terms of lift and drag coefficients and aerodynamic efficiency. The simulations have been launched on the computer cluster of the SCoPE supercomputing centre at the University of Naples "Federico II," using up to 120 CPUs in parallel.

4.1. Simulation Setup. The rotating motion of the FR was simulated using the overset/chimera mesh methodology with distance-weighted interpolation method. This method, which is especially suitable for rotational movements, uses an interpolation factor inversely proportional to the distance from acceptor cell to donor cell, as indicated in CD adapco User's Guide [18].

Hybrid mesh approach, coupling unstructured and structured mesh, has been used for all the simulations. The computational domain contains two regions: the background, nonrotating, region and the overlapped, rotating, region (Figure 5). For the background and overlapped region, an unstructured grid approach was used, while a structured boundary layer mesh was created near the FR surface. The choice of hybrid mesh approach is justified by the fact that this is a suitable compromise between accuracy and computational effort compared with the Cartesian mesh, as shown in the 2D preliminary study reported in De Marco et al. [11]. Furthermore the grid set up allowed a nondimensional wall distance ($y+$) value approximately equal to 1.0.

The chosen URANS-solving algorithm uses a first-order forward Euler scheme for the temporal discretization, an implicit element-based finite volume method, and a segregated flow approach with second-order upwind discretization of the convective terms. A fully turbulent approach with k-ω Shear Stress-Transport (SST) turbulence model has been used (a comparison with other turbulence model is reported in Figure 9). All of the properties of the numerical solver are summarized in Table 3.

It has to be noted that the simulation time step is a function of the angular speed Ω. For the convergence of the numerical scheme, as a rule of thumb, there is a limitation on the maximum cell-based Courant-Friedrichs-Lewy (CFL) number in a time step. Therefore, the higher the angular speed the lower the time step.

4.2. Computational Domain and Boundary Conditions. A box-shaped domain has been created around the cylinder

Table 3: Summary of the numerical simulation setup.

Pressure link	Pressure	Convection term	Temporal discretization	Time step (s)	Iteration per time step	Turbulence model	Overset interpolation scheme
Simple	Standard	2nd order	1st order	Function of angular speed (Ω)	11	k-ω SST	Distance weighted

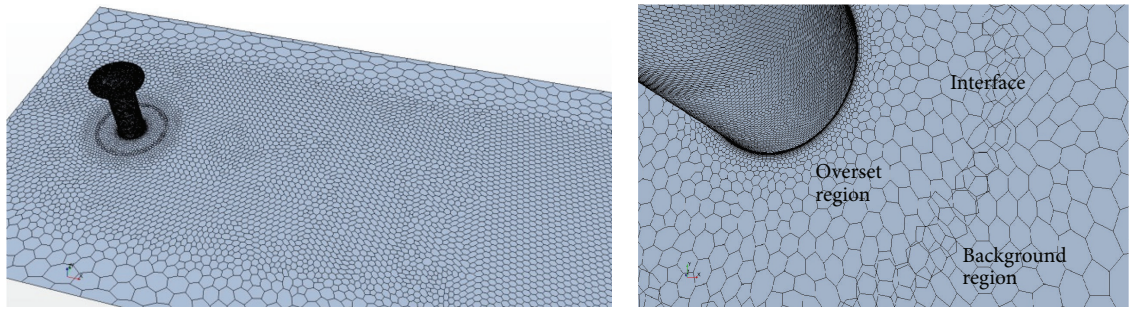

(a) (b)

Figure 5: Section of the computational grid (a). Close-up views of the hybrid mesh (b).

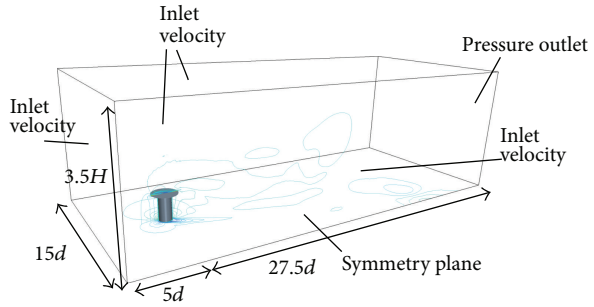

Figure 6: Boundary conditions and domain dimensions in function of the main dimensions of FR (H, d).

geometry, as seen in Figure 6. In order to reduce the computational effort, only half the domain has been considered and a symmetry plane has been assumed, containing the cylinder axis and parallel to the free stream velocity. A velocity inlet boundary condition has been set on the front side of the domain with a prescribed velocity: this inlet velocity also has been used to control the SR of the rotor, keeping constant its angular speed Ω. On the bottom and the top side of the domain, a symmetry boundary condition also is used. On the rear side of the domain surface, a pressure outlet boundary condition has been imposed with a relative pressure of value 0 Pa. An axial-symmetrical zone surrounding the rotor had to be modeled, overlapping the rotating mesh (fixed with the rotor) and the underlying nonmoving mesh domain. This turned out to be a necessary grid treatment for using the overset mesh methodology.

4.3. Numerical Uncertainty Analysis. In order to assess the numerical setup and to evaluate the simulation numerical uncertainty U_{SN}, a verification study has been performed.

The benchmark experimental data are derived from Badalamenti and Prince [8, 12] and are related to an FR with AR = 5.1 (cylinder height H = 0.45 m), diameter of d = 0.0889 m, and the Thom disk, on the top of this FR, with d_e = 0.1778 m (corresponding to d_e/d = 2.0).

According to the Oberkampf and Blottner [19], verification is defined as a process for assessing simulation numerical uncertainty U_{SN}. The simulation numerical error and uncertainty are composed of a grid convergence error (δ_G), iterative convergence error (δ_I), time step convergence error (δ_{TS}), and other parameters (δ_P). Therefore the numerical error is the sum:

$$\delta_{SN} = \delta_G + \delta_I + \delta_{TS} + \delta_P; \quad (1)$$

and the simulation numerical uncertainty is given by the formula

$$U_{SN}^2 = U_G^2 + U_I^2 + U_{TS}^2 + U_P^2, \quad (2)$$

where U_G, U_I, U_{TS}, and U_P are the uncertainties arising from the grid, iterative, time step, and other parameters, respectively (see Stern et al. [20]).

The numerical uncertainty evaluation was performed using two different methods: the grid convergence index (GCI) method and the correction factor (CF) method. The general form of the uncertainty evaluation, based on the generalized Richardson extrapolation (RE) method, can be written as follows:

$$U_k = F_S\left(\frac{\varepsilon_{21_k}}{r_k^{p_k} - 1}\right), \quad (3)$$

where ε_{21_k} is the solution changes for the k-input parameter between the solutions (fine (S_{1k}) to medium (S_{2k}) and coarse (S_{3k})), r_k is the constant refinement ratio (recommended

values between $\sqrt{2}$ and 2), p_k is the observed order of accuracy, and F_S is the safety factor. Furthermore, another parameter is the convergence ratio (R_k), which provides information about the convergence/divergence of a solution. The R_k value was determined by the following ratio:

$$R_k = \frac{\varepsilon_{21_k}}{\varepsilon_{32_k}}. \tag{4}$$

The two different solution verification methods used in this study differ in the choice of safety factor (F_S).

The GCI method proposed by Roache [21, 22] is used extensively and it is recommended, for example, by the American Society of Mechanical Engineers (ASME) [23] and the American Institute of Aeronautics and Astronautics (AIAA) [24]. Roache recommended for careful grid studies (three or more grids analyzed) 1.25 as the F_S value.

The other method used is the CF described in Stern et al. [20] that uses a variable value of F_S. In the CF method, unlike in the GCI method, the uncertainty of the error depends on how close the solutions are to the asymptotic range. The expressions to assess the uncertainties were reported by Wilson et al. [25].

The verification study has been carried out for the critical points of SR = 2.0 and SR = 2.5, in terms of C_D estimation error.

The iterative uncertainties are estimated by the fluctuations of the time-history of the results in the last few periods, as indicated in Stern et al. [20]. Specifically, as reported in (5), U_I are estimated by half the difference of the maximum value (S_U) and the minimum value (S_L) of the final time-history of the results:

$$U_I = \left| \frac{1}{2} \left(S_U - S_L \right) \right|. \tag{5}$$

Then, the grid uncertainty has been evaluated by the following expressions, that is, (6) for the GCI method and (7) for the CF method:

$$U_k = 1.25 \cdot \left| \frac{\varepsilon_{21_k}}{r_k^{p_k} - 1} \right| \tag{6}$$

$$U_k = \begin{cases} \left[9.6 \left(1 - C_k \right)^2 + 1.1 \right] \left| \dfrac{\varepsilon_{21_k}}{r_k^{p_k} - 1} \right|, & \left| 1 - C_k \right| < 0.125 \\ \left[2 \left| 1 - C_k \right| + 1 \right] \left| \dfrac{\varepsilon_{21_k}}{r_k^{p_k} - 1} \right|, & \left| 1 - C_k \right| \geq 0.125, \end{cases} \tag{7}$$

where F_S is equal to 1.25 and C_k is the correction factor. Verification results using three systematically refined grids with the refinement ratio (r_G) equal to $\sqrt{2}$ are shown in Table 5. The grid sizes range from 0.9 M to 1.9 M grid points and the three grids tested are shown in Table 4.

Because $0 < R_G < 1$, monotonic convergence is achieved for C_L and C_D, where R_G is convergence ratio for the grid, calculated according to (4). The uncertainty values are reported in Table 5.

Table 4: The three grids tested.

Grids		Cells
Grid A	Coarse	$0.933 \cdot 10^6$
Grid B	Medium	$1.320 \cdot 10^6$
Grid C	Fine	$1.867 \cdot 10^6$

The values of simulation uncertainty reported in Table 5 show that U_{SN} for C_D is higher than U_{SN} for C_L, due to much larger errors in the estimation of C_D than of C_L for SR = 2.0 and SR = 2.5.

Iterative convergence is achieved for all simulations and U_I is found to be negligible with respect to grid errors, similarly to what happens in other engineering applications (e.g., Wilson et al. [26] and Xing et al. [27]).

Moreover, the verification procedure cannot be completed with the validation phase due to the lack of experimental uncertainty data. Therefore, only the results related to simulation numerical uncertainty are reported in Table 5.

The numerical results of the verification study have been compared with the experimental data, as shown in Figure 7. The comparison highlighted that no significant improvement in the C_L and C_D evaluation is detected between coarse, medium, and fine mesh case. However, increasing the grid points increases the calculation effort, as shown in Figure 8.

For the reasons mentioned above, the grid of Case B has been assumed as the reference mesh. This grid guarantees an acceptable solution without an excessive computational effort (such as in Case C).

The comparison between experimental data and numerical results for SR in the range from 0.0 to 2.5, reported in Figure 9, shows a good agreement in particular for C_L. Regarding C_D, the CFD simulations give reliable results for SR < 1.5 and the error increases at higher values of SR, likewise highlighted in Thouault et al. [13] and Da-Qing et al. [5].

As shown in Table 5, it can be observed that for C_D the comparison error (E) is much greater than U_{SN}. According to Oberkampf and Blottner [19] and Stern et al. [20], it can be said that when E is much greater than the uncertainty, it is necessary to improve the simulations models. It is well known that one of the main sources of the modeling simulation error is the turbulence models. Nevertheless, as highlighted in Figure 9, comparing the different two-equation turbulence models, that is, k-ω SST and Realizable k-ε, no significant differences are appreciable. The k-ω SST is used as turbulence model for all the subsequent simulations; however a different simulation approach is required for an accurate C_D evaluation at high SR.

5. Results

The results of the simulations, performed into the variable ranges indicated in Table 2, are reported in terms of the so-called response curves. These curves, shown in Figure 10, represent the values of C_L and C_D and aerodynamic efficiency, keeping constant d_e/d of the FR. This representation is useful because it permits us to clearly recognize the relationships

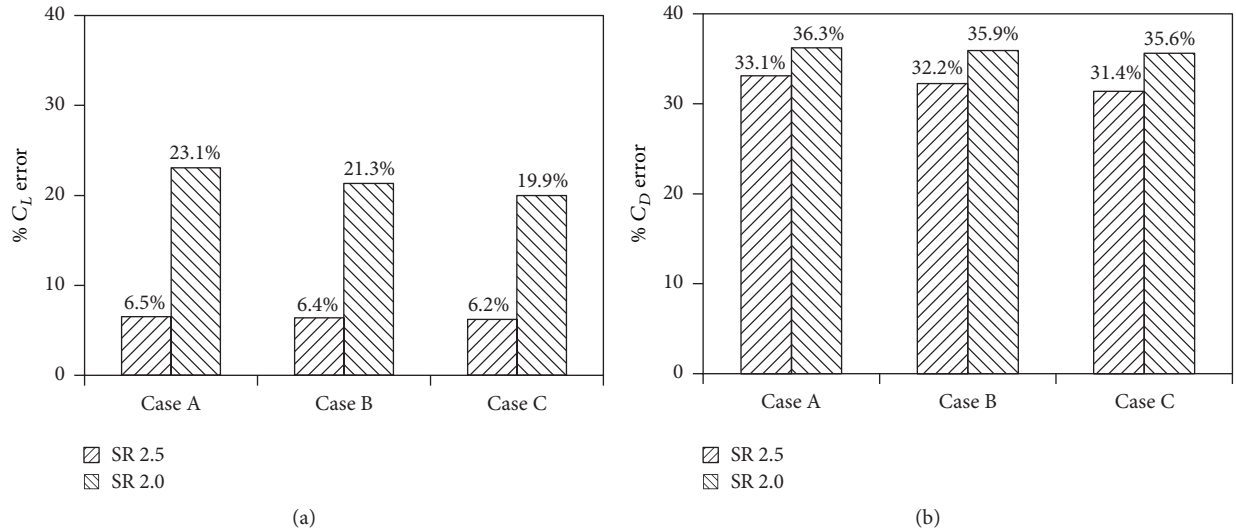

Figure 7: C_L and C_D percentage error between numerical (three mesh cases tested) and experimental data at SR = 2.0 and 2.5.

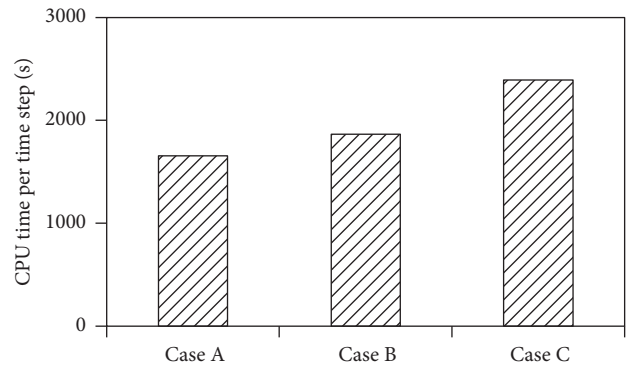

Figure 8: Computational time required for the grids tested.

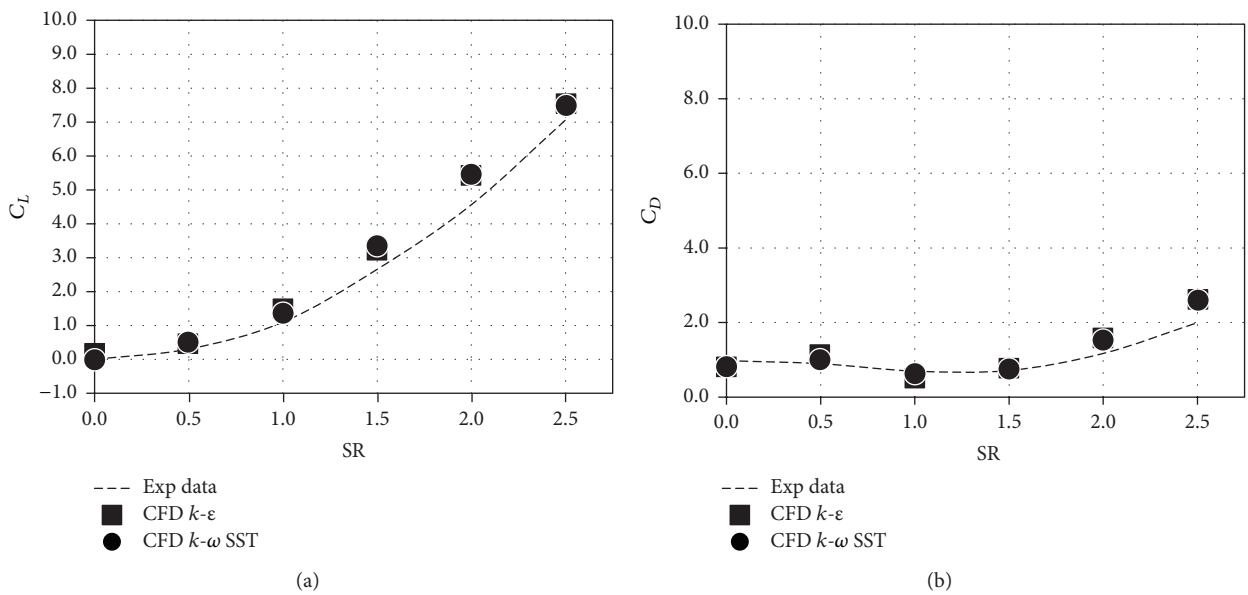

Figure 9: Comparison between CFD results and experimental data for lift (a) and drag (b) coefficient using mesh Case B and two different turbulence models.

Table 5: Grid and iterative uncertainty for C_L and C_D at the two different SRs.

	SR	Grids	Grid ratio	R_G	P_G	$1 - C_G$	% U_G GCI	% U_G CF	% U_I	% U_{SN}	% $\|E\|$
C_L	2.0	A-B-C	$\sqrt{2}$	0.80	−0.65	1.20	8.91	4.26	0.26	8.91	19.30
	2.5	A-B-C	$\sqrt{2}$	0.96	−0.12	1.04	4.40	3.23	0.55	4.43	6.24
C_D	2.0	A-B-C	$\sqrt{2}$	0.97	−0.04	1.01	20.06	15.60	1.37	20.11	36.23
	2.5	A-B-C	$\sqrt{2}$	0.96	−0.13	1.04	19.18	14.02	2.15	19.30	31.36

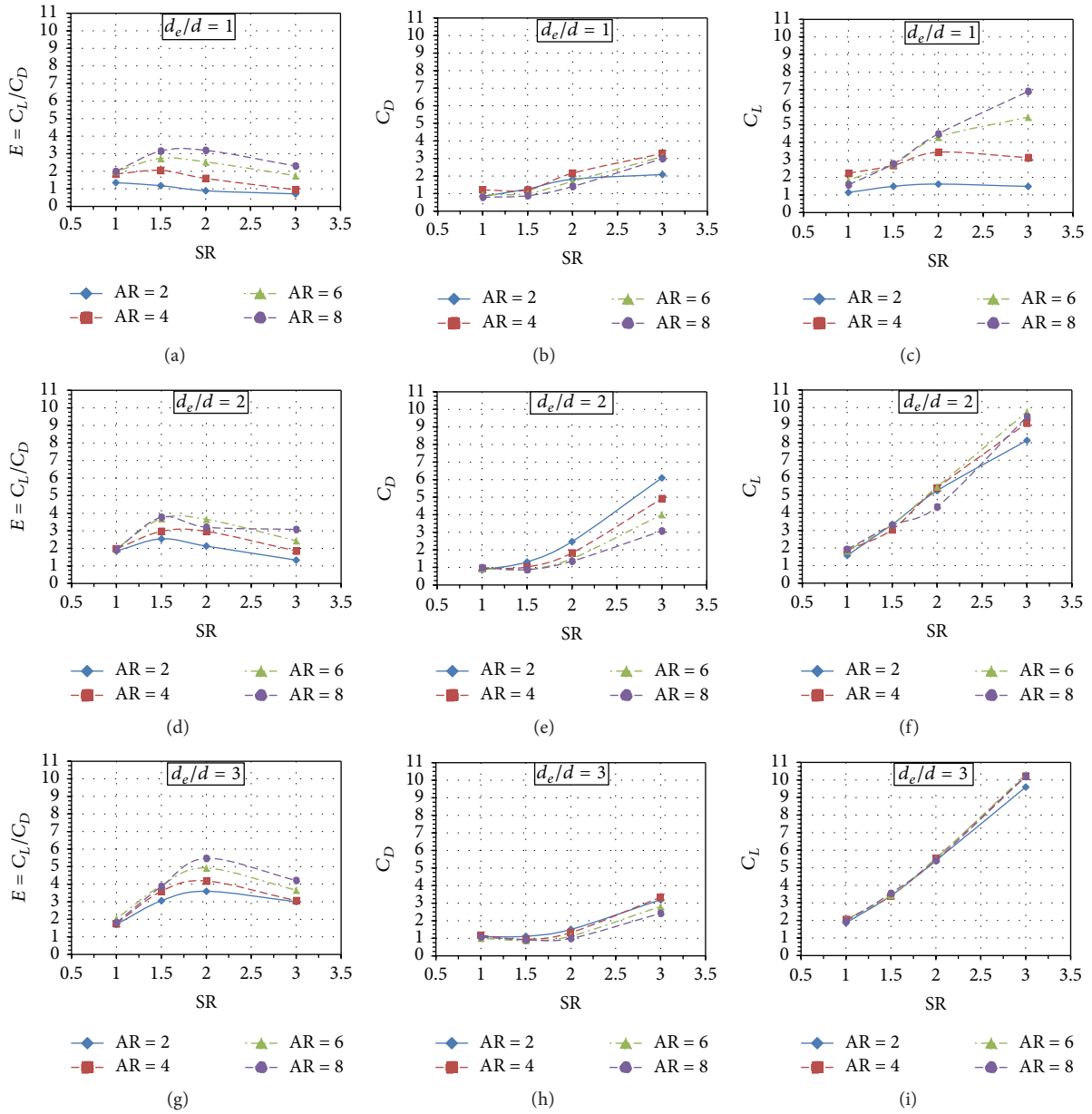

Figure 10: Response curves for C_L, C_D and aerodynamic efficiency (E) at various SR, AR, and d_e/d for FR.

between geometrical (AR, d_e/d) and functional parameters (SR) with FR performances (C_L, C_D, and aerodynamic efficiency).

The response curves in Figure 10 show that C_L is mainly influenced by the SR of the FR: as expected, high values of SR cause large value of C_L due to higher circulation around the cylinder. Keeping constant the value of d_e/d, the amount of C_L increases for high value of AR, but this trend reduces for high values of d_e/d. Also, simulations confirm beneficial effects of the FR's end plate on its performance. Referring to

C_D the ability of larger end plates to reduce the induced drag component is confirmed, as shown in Figure 10. The reason for these improvements can be due to an effect similar to increasing the AR values.

About the variation of C_D with SR, this has the same behavior of C_L, while C_D decreases as AR increases, as for a typical aircraft wing. The maximum absolute value of the FR aerodynamic efficiency rises and translates to higher SR values, when AR and d_e/d increase too.

6. Surrogate Model for the Lift and Drag Coefficients

C_L and C_D equations in (8) summarize the results of the extensive numerical analyses on the behavior of FR. These equations represent a surrogate model which can be used to predict the performance of the FR in relation to SR, AR, and d_e/d. This model is an effective mathematical tool for the preliminary design of FR.

The ratio of these two formulas allows evaluating the aerodynamic efficiency of such devices. In both equations, the coefficients a_{ijk} and b_{ijk} transform geometrical and functional FR's parameters into C_L and C_D. The values of a_{ijk} and b_{ijk} coefficients are presented in Table 6. The coefficients of the matrices a_{ijk} and b_{ijk} have been obtained by applying a least-squares root fit procedure to the numerical results, similar to the optimization techniques used to find a set of design parameters, as described in Balsamo et al. [28]:

$$C_L = \sum_{i=1}^{4}\sum_{j=1}^{4}\sum_{k=1}^{3} a_{ijk}\mathrm{SR}^i\mathrm{AR}^j\left(\frac{d_e}{d}\right)^k$$
$$C_D = \sum_{i=1}^{4}\sum_{j=1}^{4}\sum_{k=1}^{3} b_{ijk}\mathrm{SR}^i\mathrm{AR}^j\left(\frac{d_e}{d}\right)^k. \quad (8)$$

The validity of these equations is strictly related to the range of the variables analyzed: $1.0 \le \mathrm{SR} \le 3.0$, $2.0 \le \mathrm{AR} \le 8.0$, and $1.0 \le d_e/d \le 3.0$.

A test of the reliability of the surrogate model has been performed using the experimental data available in Pearson [15] relevant to FR with AR = 5.0 and d_e/d = 1.5. These values were used as input for (8). The comparison between experimental data and the predicted results is shown in Figure 11 and it can be noted that C_L is correctly estimated, while C_D is overestimated for values of SR, which are greater than 2.5. This discrepancy, which is due to the higher uncertainty on the simulated drag results, is less critical in the perspective of marine applications. In fact as indicated above, the SR values of interest in this field are not larger than 3.0, often around 2.0.

7. Flettner Rotor as Ship Propulsion Device

To evaluate the potentiality of the FRs as marine propulsion devices, it is important to consider that for FR on a ship the resulting wind speed is the vector sum of the environmental wind and the ship speed. If the resulting wind relative to the ship coordinate system is coming from the bow quarter

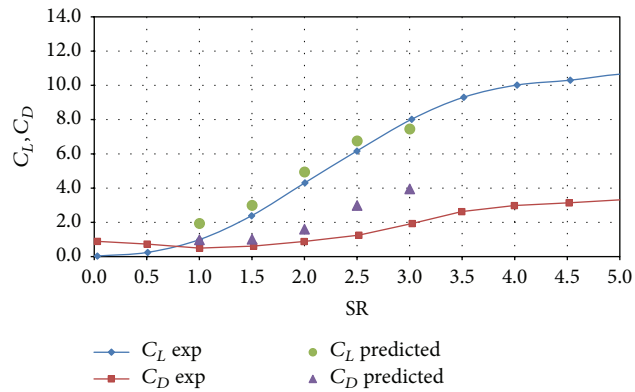

Figure 11: Comparison of experimental and predicted values of C_L and C_D for FR with AR = 5.0 and d_e/d = 1.5.

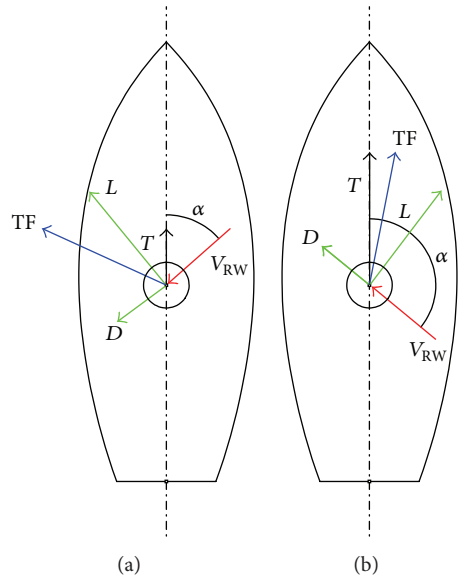

Figure 12: Total force and thrust delivered by FR at different apparent wind directions: from bow quarter (a), from stern quarter (b).

direction as illustrated in Figure 12(a), D will have a negative contribution to the resultant thrust (T). In this case, a lower drag will of course be beneficial. However, if the resulting wind is from the stern quarter direction as depicted in Figure 12(b), then D also contributes to T: under this circumstance a high drag is not disadvantage.

In Figures 12(a) and 12(b), TF is the resultant of L and D, V_{RW} the relative wind velocity, T the effective thrust, and α the apparent wind angle. Ultimately, for a geometrically well-defined FR, the resultant thrust depends on the relative wind velocity, on the apparent wind angle, and on the angular speed Ω of the FR. Obviously, the relation between V_{RW} and Ω is quantified by SR.

Figure 13 shows the values of C_T and T resulting from the polynomials whose coefficients are shown in Table 6.

As strongly suggested by Figure 13, the thrust has been evaluated at the maximum SR simulated in the study

Table 6: The values of a_{ijk} and b_{ijk} coefficients reported in (8).

i	j	k	a_{ijk}	b_{ijk}	i	j	k	a_{ijk}	b_{ijk}
0	0	0	46.756	−79.919	1	0	0	−89.785	140.718
0	0	1	−78.301	70.071	1	0	1	140.010	−125.048
0	0	2	20.282	−15.268	1	0	2	−35.672	27.377
0	1	0	−37.846	60.030	1	1	0	77.607	−104.703
0	1	1	60.058	−50.611	1	1	1	−112.204	89.137
0	1	2	−15.301	11.013	1	1	2	27.977	−19.292
0	2	0	8.096	−11.649	1	2	0	−16.461	20.215
0	2	1	−11.874	9.810	1	2	1	22.038	−17.098
0	2	2	2.987	−2.141	1	2	2	−5.409	3.698
0	3	0	−0.460	0.669	1	3	0	0.915	−1.155
0	3	1	0.639	−0.558	1	3	1	−1.152	0.964
0	3	2	−0.160	0.121	1	3	2	0.280	−0.207
i	j	k	a_{ijk}	b_{ijk}	i	j	k	a_{ijk}	b_{ijk}
2	0	0	38.547	−76.506	2	0	0	−4.895	11.799
2	0	1	−62.545	69.271	2	0	1	8.642	−10.539
2	0	2	16.266	−15.189	2	0	2	−2.294	2.290
2	1	0	−37.556	57.951	2	1	0	5.190	−9.412
2	1	1	54.801	−49.793	2	1	1	−7.946	8.065
2	1	2	−13.704	10.709	2	1	2	2.016	−1.716
2	2	0	8.153	−11.180	2	2	0	−1.154	1.831
2	2	1	−10.753	9.493	2	2	1	1.556	−1.547
2	2	2	2.627	−2.034	2	2	2	−0.383	0.327
2	3	0	−0.440	0.636	2	3	0	0.060	−0.104
2	3	1	0.534	−0.531	2	3	1	−0.073	0.086
2	3	2	−0.128	0.113	2	3	2	0.018	−0.018

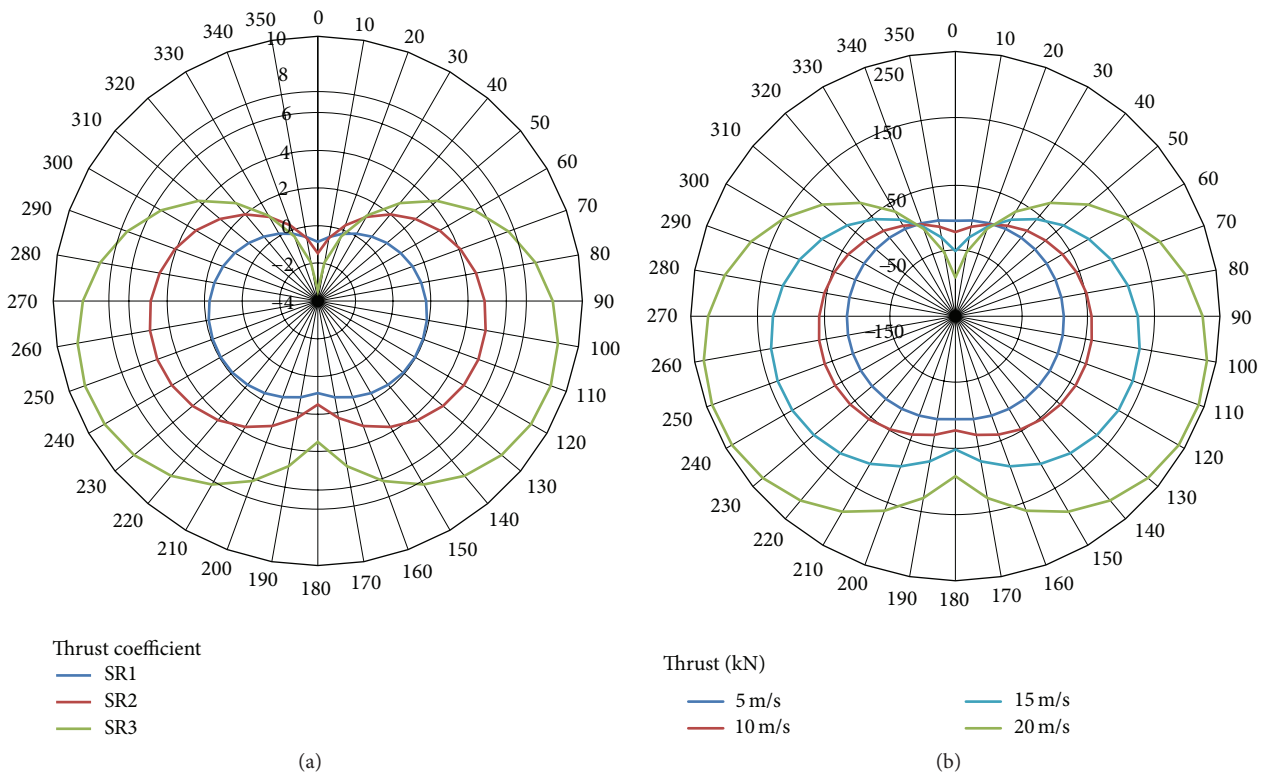

Figure 13: In (a) C_T for a defined FR geometry (H = 28.0 m, d = 4.0 m) at different values of SR and apparent wind angle. In (b) thrust values delivered by the FR for different magnitude of relative wind velocity (fixed SR = 3).

(SR = 3.0) and referring to FR whose diameter and height were 4.0 m and 28.0 m, respectively. These dimensions are consistent with the ship taken into consideration: a product tanker 205 m long at waterline and dislocating 74983 t. Towing tank tests of this ship indicate that the resistance at 10 kn and 12 kn is 354 kN and 500 kN, respectively.

Therefore the comparison of resistance of a ship with the thrust data, as shown in Figure 13, highlights that a couple of FRs, as few as 20 kn of V_{RW}, are able to give, in a wide range of angles of apparent wind, a thrust whose magnitude is 0.3 and 0.2 times the resistance of a ship at 10 kn and 12 kn, respectively.

The aim of these considerations is a rough evaluation of the potentiality of the FR as a marine propulsion device. For a more comprehensive analysis of the FR effectiveness, more aspects have to be taken into account. These include, for instance, the asymmetric hydrodynamic flow condition produced by the transversal component of TF (heeling and drift angle), extra rudder drag due to the aerodynamic yaw moment, and the reduced efficiency of FR due to the ship motions.

8. Conclusions

In this paper, a systematic approach to identify the most influencing parameters on FR performance and the applicability of such device for marine application has been presented. Results from the numerical simulations have been used to achieve a surrogate model useful for preliminary FR designs.

The uncertainty analysis shows that the highest numerical uncertainty and error are for C_D (U_{SN} = 20.1%, E = 36.2%), with respect to C_L (U_{SN} = 8.9%, E = 19.3%). Furthermore, it has been observed that the main source of numerical uncertainty is due to the grid. The C_D error and numerical uncertainty trend seems to be related to the limits of the turbulence models used, that is, k-ω SST and Realizable k-ε. Reasonably, the Large Eddy Simulation (LES) analysis should be used for an accurate evaluation of C_D, in particular at high SR.

Regarding the capability of FR to act as a propulsion device, it is confirmed that, in terms of magnitude, C_L and aerodynamic efficiency of FR is much higher than the values given by a wing of comparable aspect ratio.

Finally, the potentiality of the FR as a marine propulsion device, here evaluated on a tanker ship, highlights that, in a wide range of wind angles, a couple of FR can give a thrust whose magnitude is up to 30% of the ship resistance in the range of operational speed. Also, the assessment of the aerodynamic efficiency is less significant than the evaluation of each of the aerodynamic force components, as the drag gives a positive contribution to the thrust in a wide range of apparent wind angles.

Symbology and Abbreviations

α:	Apparent wind angle (deg)
A:	Reference area ($H * d$) (m^2)
AR = H/d:	Aspect ratio
$C_D = D/0.5\rho AU^2$:	Drag coefficient
$C_L = L/0.5\rho AU^2$:	Lift coefficient
$C_T = T/0.5\rho AU^2$:	Thrust coefficient
CFL number:	Courant-Friedrichs-Lewy number
C_k:	Correction factor
CF method:	Correction factor method
D:	Drag (N)
d:	Cylinder diameter (m)
d_e:	End plate diameter (m)
δ_I:	Iteration convergence error
δ_G:	Grid convergence error
δ_{TS}:	Time step convergence error
δ_{RE}:	Error evaluated by RE method
DWT:	Dead weight tonnage (t)
ε_{kij}:	Solution change
E:	Comparison error
f:	Frequency (Hz)
F_S:	Factor of safety
FR:	Flettner rotor
GCI:	Grid convergence index
H:	Cylinder length (m)
L:	Lift (N)
LES:	Large Eddy Simulation
ν:	Dynamic viscosity (Pa s)
Ω:	Angular velocity (rad/s)
ρ:	Air density (kg/m^3)
p_k:	Estimated order of accuracy
Re = Ud/ν:	Reynolds number
RE:	Richardson extrapolation method
r_k:	Refinement ratio
SR = $\Omega d/2U$:	Spin ratio
St = fd/U:	Strouhal number
T:	Effective thrust (N)
TF:	Total force (N)
U:	Free stream or flux velocity (m/s)
U_G:	Grid uncertainty
U_I:	Iteration uncertainty
U_{SN}:	Simulation uncertainty
U_{TS}:	Time step uncertainty
URANS:	Unsteady Reynolds averaged Navier-Stokes
$y+$:	Nondimensional wall distance.

Competing Interests

The authors declare that they have no competing interests.

Acknowledgments

The authors gratefully acknowledge the availability of the Calculation Centre SCoPE of the University of Naples "Federico

II" and thanks are due to SCoPE academic staff for the given support.

References

[1] Enercon Wind Company, "Enercon E-ship 1: a wind-hybrid commercial cargo ship," in *Proceedings of the 4th Conference on Ship Efficiency*, Hamburg, Germany, September 2013.

[2] E. G. Reid, "Tests of rotating cylinders," Techinical Notes NACA 209, 1924.

[3] A. Thom, "Effects of discs on the air forces on a rotating cylinder," Reports & Memoranda 1623, Aerospace Research Council, 1934.

[4] M. W. Swanson, "The Magnus effect: a summary of investigations to date," *Journal of Basic Engineering*, vol. 83, no. 3, pp. 461–470, 1961.

[5] L. Da-Qing, M. Leer-Andersen, and B. Allenström, "Performance and vortex formation of Flettner rotors at high Reynolds numbers," in *Proceedings of 29th Symposium on Naval Hydrodynamics*, Gothenburg, Sweden, August 2012.

[6] J. Seifert, "A review of the Magnus effect in aeronautics," *Progress in Aerospace Sciences*, vol. 55, pp. 17–45, 2012.

[7] S. Mittal and B. Kumar, "Flow past a rotating cylinder," *Journal of Fluid Mechanics*, vol. 476, pp. 303–334, 2003.

[8] C. Badalamenti and S. A. Prince, "Vortex shedding form a rotating circular cylinder at moderate subcritical reynolds numbers and high velocity ratio," in *Proceedings of the 26th Congress of International Council of the Aeronautical Sciences (ICAS '08)*, Anchorage, Alaska, USA, September 2008.

[9] E. R. Gowree and S. A. Prince, "A computational study of the aerodynamics of a spinning cylinder in a crossflow of high Reynolds number," in *Proceedings of the 28th Congress of the International Council of the Aeronautical Sciences (ICAS '12)*, pp. 1138–1147, Brisbane, Australia, September 2012.

[10] L. Prandtl, "The Magnus effect and wind-powered ships," *Naturwissenschaften*, vol. 13, pp. 1787–1806, 1925.

[11] A. De Marco, S. Mancini, and C. Pensa, "Preliminary analysis for marine application of Flettner rotors," in *Proceedings of the 2nd International Symposium on Naval Architecture and Maritime (INT-NAM '14)*, Istanbul, Turkey, October 2014.

[12] C. Badalamenti and S. A. Prince, "Effects of endplates on a rotating cylinder in crossflow," in *Proceedings of the 26th AIAA Applied Aerodynamics Conference*, Honolulu, Hawaii, USA, August 2008.

[13] N. Thouault, C. Breitsamter, N. A. Adams, J. Seifert, C. Badalamenti, and S. A. Prince, "Numerical analysis of a rotating cylinder with spanwise disks," *AIAA Journal*, vol. 50, no. 2, pp. 271–283, 2012.

[14] K. C. Morisseau, "Marine application of magnus effect devices," *Naval Engineers Journal*, vol. 97, no. 1, pp. 51–57, 1985.

[15] D. R. Pearson, "The use of flettner rotors in efficient ship design," in *Proceedings of the Influence of EEDI on Ship Design Conference*, London, UK, September 2014.

[16] M. Traut, P. Gilbert, C. Walsh et al., "Propulsive power contribution of a kite and a Flettner rotor on selected shipping routes," *Applied Energy*, vol. 113, pp. 362–372, 2014.

[17] A. De Marco, S. Mancini, C. Pensa, R. Scognamiglio, and L. Vitiello, "Marine application of flettner rotors: numerical study on a systematic variation of geometric factor by DOE approach," in *Proceedings of the 6th International Conference on Computational Methods in Marine Engineering (MARINE '15)*, vol. 1, Rome, Italy, June 2015.

[18] CD-Adapco, *Star-CCM+ User Guide*, 2015.

[19] W. L. Oberkampf and F. G. Blottner, "Issues in computational fluid dynamics code verification and validation," *AIAA Journal*, vol. 36, no. 5, pp. 687–695, 1998.

[20] F. Stern, R. V. Wilson, H. W. Coleman, and E. G. Paterson, "Comprehensive approach to verification and validation of CFD simulations—part 1: methodology and procedures," *Journal of Fluids Engineering*, vol. 123, no. 4, pp. 793–802, 2001.

[21] P. J. Roache, *Verification and Validation in Computational Science and Engineering*, Hermosa, New Mexico, NM, USA, 1998.

[22] P. J. Roache, "Code verification by the method of manufactured solutions," *Journal of Fluids Engineering*, vol. 124, no. 1, pp. 4–10, 2002.

[23] I. B. Celik, U. Ghia, P. J. Roache, C. J. Freitas, H. Coleman, and P. E. Raad, "Procedure for estimation and reporting of uncertainty due to discretization in CFD applications," *Journal of Fluids Engineering*, vol. 130, no. 7, 2008.

[24] R. Cosner, W. L. Oberkampf, C. L. Rumsey, C. Rahaim, and T. Shih, "AIAA Committee on standards for computational fluid dynamics: status and plans," AIAA Paper 2006-889, American Institute of Aeronautics and Astronautics, Reno, Nev, USA, 2006.

[25] R. Wilson, J. Shao, and F. Stern, "Discussion: criticism of the correction factor," *Journal of Fluids Engineering*, vol. 126, no. 4, pp. 704–706, 2004.

[26] R. V. Wilson, F. Stern, H. W. Coleman, and E. G. Paterson, "Comprehensive approach to verification and validation of CFD simulations—part 2: application for RANS simulation of a cargo/container ship," *Journal of Fluids Engineering*, vol. 123, no. 4, pp. 803–810, 2001.

[27] T. Xing, P. Carrica, and F. Stern, "Computational towing tank procedures for single run curves of resistance and propulsion," *Journal of Fluids Engineering*, vol. 130, no. 10, Article ID 101102, 14 pages, 2008.

[28] F. Balsamo, F. De Luca, and C. Pensa, "A new logic for controllable pitch propeller management," in *Proceedings of the 14th International Congress of the International Maritime Association of the Mediterranean (IMAM '11)*, vol. 2, pp. 639–647, Genoa, Italy, September 2011.